Rolling Microswarms along Acoustic Virtual Walls

Zhiyuan Zhang
https://orcid.org/0000-0001-6019-1863
Alexander Sukhov
Helmholtz Institute Erlangen–Nürnberg for Renewable Energy (IEK-11)
Jens Harting
Forschungszentrum Julich https://orcid.org/0000-0002-9200-6623
Paolo Malgaretti
https://orcid.org/0000-0002-1201-451X
Daniel Ahmed (dahmed@ethz.ch)
ETH Zurich https://orcid.org/0000-0002-0224-5293

Article

Keywords: Rolling, Microswarm, Micromanipulation, Acoustics, Magnetics

Posted Date: April 12th, 2022

DOI: https://doi.org/10.21203/rs.3.rs-1505456/v1

Rolling Microswarms along Acoustic Virtual Walls

Zhiyuan Zhang[1], **Alexander Sukhov**[2], **Jens Harting**[2,3], **Paolo Malgaretti**[2], **and Daniel Ahmed**[1,*]

[1] Acoustic Robotics Systems Laboratory, Institute of Robotics and Intelligent Systems, Department of Mechanical and Process Engineering, ETH Zurich, Zurich, 8803, Switzerland.

[2] Helmholtz Institute Erlangen–Nürnberg for Renewable Energy (IEK-11), Forschungszentrum Jülich, Nuremberg, 90429, Germany.

[3] Department of Chemical and Biological Engineering and Department of Physics, Friedrich-Alexander-Universität Erlangen-Nürnberg, Nuremberg, 90429, Germany.

*Correspondence and requests for materials should be addressed to D.A. (e-mail: dahmed@ethz.ch).

Abstract

Rolling is a ubiquitous mode of transport utilized by both living organisms and engineered systems. Rolling, on the microscale, has become particularly interesting for the manipulation of microswarms, since enacting such motion does not require special prefabrication techniques. However, rolling motion has to date been restricted by the need for a physical boundary to break the spatial homogeneity of surrounding mediums, which limits its prospects for microswarm navigation and cargo delivery to locations with no boundaries. Here, in the absence of real physical boundaries, we show that chain-shaped microswarms can undergo rolling motion along virtual walls in the aqueous medium, impelled by a combination of magnetic and acoustic fields. A rotational magnetic field causes individual particles to self-assemble and rotate, while the pressure nodes generated by an acoustic standing wave field serve as virtual walls. The acoustic radiation force pushes the rotating microswarms towards a virtual wall and provides the reaction force needed to break their fore-aft motion symmetry and induce rolling. We develop an experiment-supported theoretical model to quantify the net displacement generated by rolling. Finally, we demonstrate that rolling can be achieved along arbitrary trajectories by dynamically switching the orientation of the virtual walls and the rotational directions of the magnetic field. Consequently, the concept of reconfigurable virtual walls developed here overcomes the fundamental limitation of a physical boundary being required for universal rolling movements.

Keywords: Rolling | Microswarm | Micromanipulation | Acoustics | Magnetics

Introduction

Classically, rolling is regarded as a type of motion that combines the rotational motion of an object with its translation across a physical boundary. Rolling motion is ubiquitous throughout nature, occurring at scales from the macro to the nano. Tumbleweeds [1], web-toed salamanders [2], and golden wheeling spiders [3] all utilize rolling to disperse seeds or avoid predators. Vampire amoebae [4] and neutrophils [5] adopt rolling to propel along cellular or vascular walls. The rolling motion is also commonly used in engineered systems such as trains, automobiles, and robots [6, 7]. Being well-established as an effective transport mechanism, rolling is also increasingly studied for the navigation and manipulation of artificial objects at the micro/nano-scale, where viscous forces usually dominate inertial effects [8, 9].

To date, self-assembled microswarms that generally propel by means of a rolling-type motion [10–13] are becoming attractive since they do not require special prefabricated elements (e.g. sophisticated structures [14], assembly steps [15], surface modifications [16] and so on) and due to their flexible motility, which confers more degrees of freedom for navigation in lab-on-chip microsystems [17] and complex in vivo vasculature networks [18, 19]. However, to convert rotational motion into rolling motion in liquid, existing strategies predominantly rely on a physical boundary (liquid-solid interface) to introduce spatially asymmetrical hydrodynamic interactions [20–22]. Whether involving a smooth or textured surface topography, the strong dependence of these rolling strategies on the presence of a boundary is a fundamental limitation that impairs microswarm maneuverability.

In tandem, a variety of strategies for microswimmer and microswarm motility have been developed, including ones based on chemical gradients [23–27], bacterial power [28, 29], or external fields such as magnetic [30–37] and electric [38, 39] fields, as well as energy from light [40–42], heat [43, 44], and ultrasound [45–52]. Among those, strategies using magnetic and acoustic modalities are intriguing since they allow for the manipulation of micro-objects without contact, they are unscreened (in contrast to electrostatic interactions), unaffected by object opacity (in contrast to optical traps), and they can generate a broad range of forces [53–56].

Here, we report a novel strategy, based on a combination of acoustic and magnetic fields, to realize rolling of chain-shaped microswarms (microchains) along a virtual wall in liquid in the absence of real walls Fig. 1a illustrates the virtual wall concept: while a conventional microchain (grey) has to follow the boundary in order to break its motion symmetry and roll; in contrast, our microchain (green) can directly roll left-to-right along a virtual wall distant from the real physical boundary. Within our strategy, when microparticles are introduced into an acoustic standing wave field, the acoustic radiation force (ARF)

attracts and aligns them towards the pressure nodal lines that serve as the virtual walls. Then, when a rotational homogeneous magnetic field having its rotational axis perpendicular to the acoustic standing wave field is employed, neighboring magnetic particles self-assemble into multiple microchains and start rotating on account of the magnetic dipole-dipole interactions and the induced magnetic moment [11, 57] (Fig. 1b and Supplementary Movie 1). The distributed and time-varying ARF acting on the rotating microchain effectively breaks its motion symmetry and induces rolling. To further understand and describe this observation, we develop an experiment-supported model, which is consistent with our experimental data and provides significant insights into the rolling motion. Finally, by dynamically building a reconfigurable acoustic virtual wall and switching the rotational direction of the magnetic field, we achieved manipulation of microchains along arbitrary trajectories in liquid while far from real surfaces or boundaries (Fig. 1c).

Results

System design. Our experimental setup, shown in Fig. 1d, consists of an acoustic manipulation chamber and a magnetic manipulation system. During experiments, we developed two different acoustic manipulation chambers. The first one is within a confined glass capillary where an acoustic pressure nodal line can be developed at the middle of the capillary by two oppositely placed piezoelectric transducers. Within this chamber, we characterized the rolling behavior of microchains along the one-dimensional (1D) virtual wall. The second one is an open acoustic chamber which comprises a square chassis with four piezoelectric transducers that are indicated as transducer pairs $A_{1,2}$ and $B_{1,2}$ (Supplementary Fig. 1). Within this second chamber, we performed bidirectional and two-dimensional (2D) dynamic rolling. As the energy of the acoustic field scales quadratically with the excitation voltage (see **Methods** for details), the transducer pair with the higher excitation voltage will dominate the acoustic standing wave field in terms of intensity. Therefore, the orientation of the acoustic virtual walls (parallel to the x-axis or y-axis, respectively) constituted by the pressure nodal lines can be dynamically switched by tuning the excitation voltage of the originating transducers (Supplementary Fig. 2a to 2c and Supplementary Movie 2).

The magnetic manipulation system comprises a 5-axis robotic arm and a magnetic end-effector positioned around the acoustic chamber. The end-effector consists of a horseshoe-shaped gripper that uses a pair of permanent magnets (with one north pole points to the other south pole) on its sidearms to establish a homogeneous magnetic field. As the robotic arm executes a programmed rotation, the permanent magnets revolve around the chamber, generating a rotational magnetic field in the horizontal x-y plane, $\mathbf{B}(\mathrm{t}) = B_0\cos\omega t\mathbf{e}_x + B_0\sin\omega t\mathbf{e}_y$, where B_0 is the intensity of the magnetic field, ω is the angular frequency, and $\mathbf{e}_x$ and $\mathbf{e}_y$ are the unit vectors. The calculation based on the Biot-Savart law [58] and the simulation in

COMSOL Multiphysics of the magnetic intensity (see **Methods** for details) show that the magnetic field between a pair of permanent magnets is unidirectional. The magnetic field gradient is close to zero in the range of -1000 µm to +1000 µm, which is three orders of magnitude larger than the diameter of the magnetic particles used (Supplementary Fig. 2d to 2f). Control experiments have shown that in a static magnetic field, while the microchains gradually increased in length with time, no noticeable motion has been observed (Supplementary Fig. 3). Accordingly, the microchains in the central region of the acoustic chamber experience a nearly homogeneous magnetic field, and hence the magnetic field gradient does not contribute to the displacement of microchains.

Rolling Motion. To characterize the rolling motion of microchains in the combined acoustic and magnetic field, a set of 1D manipulation experiments with a variety of excitation parameters (namely varying the excitation voltage of the acoustic field and the rotational velocity of the magnetic field) has been performed in a narrow, closed glass capillary with a circular cross-section, as illustrated in Fig. 2a. In the combined presence of acoustic and magnetic fields, microchains exhibited rolling along the acoustic virtual wall (Fig. 2b). We tracked and analyzed a single microchain (with the length of 65.63 µm). Fig. 2c demonstrates the translation velocity of a microchain against the magnetic rotational velocity at excitation acoustic voltages of 10 (red) and 20 (green) V_{PP} (peak-to-peak voltage). As we increase the rotational frequency of the magnetic field, the translation velocity of the microchain increases, revealing a linear relationship, $v \propto \omega$ The translation velocity also increases with acoustic voltage (Fig. 2d), which can be attributed to a higher ARF acting on the microchains. Additionally, the translation velocity is also proportional to the length of the microchains for a fixed acoustic voltage and magnetic rotational velocity (Fig. 2e).

Bidirectional manipulation. To demonstrate the flexibility and stability of our manipulation strategy, we tested the bidirectional rolling of multiple microchains along 1D acoustic virtual walls in the open acoustic chamber (Supplementary Movie 3). In particular, we checked that the direction of rolling can be reverted immediately upon flipping the rotational direction of the magnetic field, as shown in Fig. 3a. The rotational angular velocity of microchains precisely follows the rotational frequency of the magnetic field during multiple rolling cycles (Supplementary Fig. 4) Then, the rolling microchains come to a stop instantaneously by switching off the rotation of the magnetic field. Upon switching the orientation of the acoustic standing wave field with 90 degree, the microchains move in the orthogonal direction at roughly the same speed (Fig. 3b). Additionally, Fig. 3 shows that when multiple microchains are present they may cluster and, within the same cluster, they may have different velocities. This can be due to the dispersive nature of microchain properties such as the length, shape, and magnetic moment, which further affects the interaction of microchains with the combined field and surrounding liquid. Concerning the nature of the external

fields, the translation velocity of microchains in the open acoustic chamber was also found to increase with increasing magnetic rotational velocity, stronger magnetic intensity, higher acoustic voltage, and higher acoustic frequency (Supplementary Fig. 5).

Rolling mechanism and modeling. To gain better insight into this rolling motion, we first investigated the behavior of microchains in a rotational magnetic field both without and with an acoustic standing wave field. The results of a control experiment show that in the absence of any acoustic wave fields, most of the microchains started symmetrical rotation around their geometric center upon switching on the rotational magnetic field. Although the rotation center of some microchains deviated from the geometric center, the microchains exhibited no net translational motion. (Fig. 4a) shows that the final rotational profile of a microchain resembled a circle, implying the motion symmetry was not broken. In contrast, in the presence of a 1D acoustic standing wave field, the rotating microchain exhibited not only a similar off-center rotation but also a net translation along the pressure nodal line (Fig. 4b and Supplementary Fig. 6).

We then tracked and analyzed a single microchain rotating in the combined acoustic and magnetic field with a constant magnetic rotational velocity of 12 rpm (i.e., a rotational period of 5 seconds) (Supplementary Movie 4 and Supplementary Fig. 7). Image superposition (Fig. 4c) reveals that the microchain has different angular spacings, with values decreasing in frames 1-8 (when the microchain rotated to become perpendicular to the acoustic pressure nodal line) and then increasing in frames 8-16 (when the microchain rotated to become parallel to the acoustic pressure nodal line), suggesting that in a single rotational cycle, the microchain first decelerates and then accelerates. Because the ARF acting on the microchain always points to the pressure nodal line, its effective magnitude varies according to the orientation of the chain (Supplementary Fig. 8). Meanwhile, the trajectories of the microchain's two endpoints (indicated as P_1 and P_2), geometric center (indicated as C), and rotational center (indicated as A) demonstrate that the distance l between the geometric and rotational centers varies across the rotational cycle (Fig. 4d), with a sinusoidal dependence on rotational time (Fig. 4e). When the long axis of the microchain is parallel to the virtual wall, the center of rotation nearly overlaps with the geometric center; whereas when the long axis becomes perpendicular to the virtual wall, the distance goes to its maximum value. In contrast, the tracking and analysis of a single microchain rotating in the rotational magnetic field without the acoustic standing wave field revealed no apparent rhythmic offset between the geometric and rotational centers (Supplementary Fig. 9). This finding suggests that the action of the time-varying ARF on the microchain is critical for its net displacement.

With this in mind, we developed a theoretical model to capture the net displacement of the rolling

microchains along the acoustic virtual wall. In the model, the self-assembled microchain is regarded as a uniform rigid body, as shown in Fig. 4f. According to our previous study [19], thermal agitation or Brownian motion cannot disrupt the formation of microchains, and the thermal contribution to the viscous force is negligible. We also remark that due to the small size of the microrods and their relatively small velocity, both the inertia of the particle (overdamped regime) as well as the inertia of the fluid (with a low Reynolds number) can be disregarded (Supplementary Note 1). As suggested by our data we regard the distance of the center of mass to the center of rotation as a function of time, $l(t)$. Accordingly, the time-averaged net displacement of the geometric center of the microchain, δ, can be obtained by integrating the product of the rotational time interval, dt, and the linear velocity component in the translation direction within the rotational period, T, as

$$\delta = \omega \int_0^T \sin(\omega t) l(t) \mathrm{d}t, \tag{1}$$

where $\omega = 2\pi/T$ is the angular velocity of the rotational magnetic field. By expressing $l(t)$ via its Fourier expansion, we obtain

$$l(t) = a_0 + \sum_{i=1}^{\infty} \left[a_i \cos(i\omega t) + b_i \sin(i\omega t) \right], \tag{2}$$

where a_i and b_i are the Fourier parameters. Based on the orthogonality of trigonometric functions for integration, we obtain

$$\delta = \omega b_1 \int_0^T \sin(\omega t)\sin(\omega t)\mathrm{d}t = \omega b_1 \frac{T}{2} = \pi b_1, \tag{3}$$

$$v = \frac{\delta}{T} = \frac{b_1}{2}\omega, \tag{4}$$

where b_1 is the first item of b_i, $b_1 = \frac{2}{T}\int_0^T l(t)\sin(\omega t)\mathrm{d}t$, and v is the time-averaged translation velocity. Over multiple rotational cycles, n, the total net displacement is $n \cdot \delta$.

Within the current model, the time-varying acoustic radiation force on the microchains is accounted for by the time-dependent distance $l(t)$. The model suggests that in the absence of a rotational magnetic field, the angular velocity, $\omega = 0$, and no rolling occurs. Likewise, in the absence of the acoustic standing wave field, but with the rotational magnetic field on, l, remains constant in time and hence $b_1 = 0$, leading no rolling motion. Therefore, a microchain undergoes rolling motion only when both rotational magnetic and acoustic standing wave fields are applied. To verify the model, we extracted $l(t)$ from the experimental data and fitted it with $l(t) = \tilde{l}\sin(\tilde{\omega}t)$, as shown in Fig. 4e. Using the fitting parameters, $\tilde{l}$ and $\tilde{\omega}$, and Eq. (3) and Eq. (4) the time-averaged displacement δ and velocity v of the tracked microchain (Fig. 4c) over a single rotational cycle read $\delta_{th} = 22.49$ µm and $v_{th} = 4.49$ µm/s which are consistent with the tracked experimental data of $\delta_{exp} = 22.1$ µm and $v_{exp} = 4.4$ µm/s. The model, however, does not predict

the potential factors for the rolling motion from the parameters characteristic of the combined field (such as acoustic voltage, acoustic frequency, and magnetic intensity) and the microchain length and thickness. A future work will examine the coupling effect of the combined field.

Two-dimensional dynamic manipulation. Here, we investigated the capacity of our microchains to perform 2D rolling along acoustic virtual walls. When a 2D acoustic standing wave field was developed in the open acoustic chamber, suspended microchains were aggregated into lattice-like dots and they only rotated at the acoustic pressure node points (Fig. 5a). In this condition, the 2D standing waves manifest as a local energy barrier around each nodal point and microchains cannot exhibit translational motion. Accordingly, the 2D acoustic standing wave field is employed as a transfer station to realize smooth turns and avoid positional shifts that may occur when directly switching the orientation of the 1D virtual walls.

We then manipulated the microchains to roll along a predesigned square path by manual operations (Fig. 5b). First, transducer pair A was activated at 20 V_{PP}, and transducer pair B was activated at 1 V_{PP} to build the x-axial acoustic virtual wall. Thus, the microchains executed right-to-left rolling in the counterclockwise rotational magnetic field. Later, the excitation voltage of transducer pair B was gradually raised to 20 V_{PP} to develop the 2D acoustic standing wave field and stop the microchains at the nodal point. Then, the y-axial acoustic virtual wall was built and the microchains exhibited bottom-to-top rolling upon the excitation voltage of transducer pair A was gradually reduced to 1 V_{PP}. As the microchains approached the next pressure nodal point, we gradually raised the excitation voltage of transducer pair A back to 20 V_{PP} and switched the rotational direction of the magnetic field from counterclockwise to clockwise direction. Subsequently, the excitation voltage of the transducer pair B was gradually reduced to 1 V_{PP} and the microchains exhibited left-to-right rolling. Similarly, the y-axial acoustic virtual wall was then reconstructed again and the microchains finally rolled back to their initial point from top to bottom. The dexterity of our manipulation strategy is further illustrated in Fig. 5c, where microchains roll along dynamically reconstructed acoustic virtual walls with trajectories that are depicted by the letters "E", "T", and "H" (Supplementary Movie 5). It can be expected that more precisely following of the desired trajectory will be achieved by automatically tuning the acoustic voltage through a program-controlled function generator. These demonstrations confirm the multi-particle dynamic manipulation capacity of our strategy and its potential as an efficient transportation solution.

Discussion

In this work, we reported a strategy for manipulating chain-shaped microswarms into rolling without relying on physical boundaries. Under the combination of an acoustic standing wave field and a rotational

magnetic field, magnetic particles are trapped and self-assemble into microchains that execute rolling along acoustic pressure nodal lines, which act as virtual walls. The time-varying distance between the geometric and rotational centers of the microchain, which is driven by the acoustic radiation force, accounts for the symmetry breaking and induction of rolling. We further demonstrated dexterous rolling of microchains along arbitrary trajectories, realized by dynamically constructing the virtual walls and switching the rotational direction of the magnetic field. Regarding the apparatus, we established the rotational magnetic field using a 3D-printed frame featuring several commercial permanent magnets, which is easy to construct and portable. During our experiments in the confined glass capillary, we observed three rows of rolling microchains in the capillary: one on each side rolling along the capillary boundary, and the third in the middle rolling along the virtual wall (Supplementary Fig. 10). Because all three rows of microchains can be clearly observed under a single microscope focus setting, the virtual wall is implied to be developed in the middle, far from the bottom boundary of the circular capillary. Thus, the control experiments in the capillary also confirmed realization of rolling in the absence of real walls. Our concise and experiment-supported theoretical model provides convincing explanations and insights regarding the rolling mechanism and its characterization; moreover, the $l(t)$ term can be replaced, meaning this model is not limited to rolling along an acoustic virtual wall but can generally describe any similar rolling motions.

An additional method for switching the orientation of the acoustic virtual wall is through frequency modulation of the transducers. When all four transducers were excited by an acoustic voltage of 20 V_{PP} and frequency 2.24 MHz, the developed acoustic pressure nodal line tended to be x-axial; in contrast, the same voltage with a frequency of 2.29 MHz developed a nodal line that tended to be y-axial (Supplementary Fig. 11 and Supplementary Movie 2). We posit that the alternate domination of the field by the two transducer pairs in this case is due to there being a slight difference in their respective resonant frequencies. Notably, since the spacing between acoustic pressure nodal lines is dictated by excitation frequency, higher excitation frequencies allow finer adjustment, i.e., navigation with higher spatial resolution. To realize more flexible modulation of the acoustic virtual walls and rolling in 3D space, a transducer array can be designed to establish 3D virtual walls [59–61] and incorporate a rotational magnetic field with variable rotational axes. Meanwhile, in this work, the angular frequency of the rotational magnetic field is restricted by the rotational rate of the robotic arm (0 to 40 rpm). A high-speed motor can be installed between the magnetic manipulation system and the robotic arm to increase rotational rate and so further increase the microchain rolling velocity.

Overall, rolling along a customizable acoustic virtual wall can reduce operational complexity as

compared to rolling along a real boundary, and can further provide an efficient alternative solution for propulsion over rugged terrain. Consequently, our rolling strategy will enrich microfluidic lab-on-chip technologies for achieving efficient actuation, dexterous handling, and selective stimulation of micro-objects. As acoustic and magnetic fields can readily extend into the body, we envision rolling along virtual walls to have great potential for *in vivo* medical applications.

Methods

Acoustofluidic setup. The square chassis of the acoustic chamber with dimensions $24 \times 24 \times 20$ mm is fabricated from black photopolymer resin (Standard Black, Formlabs) by 3D printing (Form 3, Formlabs). Four piezoelectric transducers (SM111, STEMINC) are orthogonally glued to the chassis. According to the technical data sheet by the manufacturer, the transducer resonance frequency is 1.5MHz $\pm$ 4%. Subsequently, the acoustic chamber is glued to a thin glass substrate. Two electronic function generators (TG1006, Aim-TTi) are connected to the two transducer pairs to generate the ultrasound waves. For the confined glass capillary chamber, a capillary with the outer diameter of 1.5 mm and the inner diameter of 1mm is embedded into a rectangular PDMS (Polydimethylsiloxane) polymer substrate, which is fabricated using the mold replica technique. And two piezoelectric transducers are glued to the PDMS lateral surfaces to establish the acoustic standing wave field.

Magnetic setup. The horseshoe-shaped gripper of the magnetic manipulation system with dimensions $44 \times 42 \times 10$ mm is fabricated from black photopolymer resin by 3D printing. To build the magnetic field, permanent magnets (S-10-05-N52N, NdFeB, Supermagnete) are symmetrically mounted on both sidearms of the gripper. To rotate the magnetic field, the magnetic device is mounted to the end of a 5-axis robotic arm (Dorna 2, Dorna Robotics). In addition, the magnetic intensity can be adjusted by adding external permanent magnets to or removing them from the sidearms (Supplementary Fig. 2f).

Experimental particles. Commercially available encapsulated magnetic polymer particles having the diameter of 1.63 µm (COMPEL, Bangs Laboratories) are utilized in our experiments. Benefitting from the high susceptibility, these particles react quickly to the external magnetic field. Since, the acoustic excitation frequency of our transducer pairs is around 1.5 MHz corresponding to acoustic wavelength, λ, around 1 mm, the size of these particles ensures the validity of the basic assumption of the particle diameter $a << \lambda$ of the Gor'kov theory.

Acoustic radiation force. When acoustic standing waves are generated in a liquid containing suspended microparticles, the acoustic radiation force which comprised of primary and secondary radiation forces will arise [62]. The primary radiation force arises from the scattering of the background acoustic standing waves

on the particle, whereas the secondary radiation force results from the scattered waves between adjacent particles. Here, we focus on the primary radiation force which plays an important role on aggregating microparticles. Based on the gradient of the Gor'kov potential [63], the time averaged primary radiation force acting on a single isolated incompressible particle in an one-dimensional acoustic standing wave field can be expressed as

$$F_{AR} = 4\pi\phi(\widetilde{\kappa},\widetilde{\rho})ka^3E_{ac}\sin(2kx), \tag{5}$$

$$\phi(\widetilde{\kappa},\widetilde{\rho}) = \frac{1}{3}\left[\frac{5\widetilde{\rho}-2}{2\widetilde{\rho}+1} - \widetilde{\kappa}\right], \tag{6}$$

$$\widetilde{\rho} = \frac{\rho_s}{\rho_0}, \widetilde{\kappa} = \frac{\kappa_s}{\kappa_0} \tag{7}$$

where a is the radius of the microparticle which is considerably smaller than the acoustic wavelength λ; ϕ is the acoustic contrast factor. The used magnetic particles have a positive contrast factor, which is estimated to be 0.29 (Supplementary Note 2); k is the wavenumber of the standing wave with the pressure field $P = P_a\cos(kx)\cos(\omega t)$, P_a denotes the pressure amplitude, x determines the position of the particle, ω is the propagating frequency; E_{ac} denotes the acoustic energy; ρ_0, ρ_s denote the density of the liquid and particle, respectively; κ_0, κ_s denote the compressibility of the liquid and particle, respectively [64].

Relationship between the acoustic radiation force and excitation voltage. In Eq. (6), the acoustic energy E_{ac} can be obtained as

$$E_{ac} = \frac{P_a^2}{4\rho_0 c_0^2} = \frac{1}{4}\rho_0 v_0^2, \tag{8}$$

where v_a is the induced acoustic velocity; c_0 denotes the speed of sound in water, 1500 m/s. In study [65], it is shown that the induced acoustic pressure amplitude P_a is linear to the applied peak-to-peak voltage, V_{PP}, of the piezoelectric transducer. Consequently, we obtain the following equation

$$F_{AR} \propto E_{ac} \propto P_a^2 \propto V_{PP}^2. \tag{9}$$

Magnetic intensity of the cylindrical permanent magnet. Based on the Biot-Savart law [58], the magnetic intensity at any points on the polar axis of the cylindrical permanent magnet can be obtained by

$$B(x) = \frac{B_r}{2}\left[\frac{L+x}{\sqrt{R^2+(L+x)^2}} - \frac{x}{\sqrt{R^2+(x)^2}}\right], \tag{10}$$

where B_r is the remanence of the magnet, for the N52N magnetic material, the reference value of remanence is 1.44 T; L and R is the length and radius of the magnet, respectively; x is the distance between the test point and the magnet. In this work, we used a pair of magnets to build the magnetic field. The total

distance, S, between the magnetic pair is 40 mm. Thus, the magnetic intensity in the rang (-20 mm, 20 mm) can be calculated as

$$B = B(x) + B(S - x). \tag{11}$$

Numerical simulation. Finite element numerical simulations are conducted using the commercial COMSOL Multiphysics software (v5.5, Burlington, MA). We perform the acoustic standing wave field simulations with the "Pressure Acoustics, Frequency Domain" module. The inward "Normal Displacement" of the "Sound Hard Boundary" is enabled to denote the oscillation from piezoelectric transducers. The simulated acoustic pressure pattern is consistent with our experimental results. For magnetic simulations, the "Magnetic Field, No Current" module is used. The material of the permanent magnet is set as N52 (Sintered NdFeB) and the magnetization model is "Relative permeability". A square airbox is employed as the calculation domain. All geometrical parameters are set as the experimental setup and the physics-controlled mesh is utilized. The simulated magnetic intensity is consistent with our numerical calculations.

Imaging and data analysis. The acoustic chamber is mounted on an inverted microscope (Axiovert 200M, ZEISS) equipped with a CCD Monochrome Camera (Photometrics Cool SNAP EZ, Boston Microscopes) and a high-speed camera (Chronos 1.4, Kron Technologies). The angular velocity and translation velocity of microchains are analysed by video analysis in ImageJ [66].

Data Availability. The datasets that support the findings of this study are available from the corresponding author upon request.

Acknowledgement

This project has received funding from the European Research Council (ERC) under the European Union's Horizon 2020 research and innovation programme grant agreement No. 853309 (SONOBOTS). P.M., A.S., and J.H. acknowledge financial support from the German Research Foundation (DFG, Project-ID 416229255 - SFB 1411).

Author contributions

D.A. conceived and supervised the project. Z.Z. performed all the experiments, data analysis, and numerical simulations. P.M., Z.Z., A.S., D.A., and J.H. contributed to the theoretical understanding. Z.Z. and D.A. contributed to the experimental design, scientific presentation, discussion, and manuscript writing.

Competing interests

The authors declare no competing financial interests.

References

1. Bar-Cohen, Y. *Biomimetics: Nature Based Innovation*. Biomimetics series (CRC Press, 2012).
2. García-París, M. & Deban, S. M. A novel antipredator mechanism in salamanders: rolling escape in hydromantes platycephalus. *J. herpetology* **29**, 149–151 (1995).
3. Armour, R. H. & Vincent, J. F. Rolling in nature and robotics: a review. *J. Bionic Eng.* **3**, 195–208 (2006).
4. Hess, S., Sausen, N. & Melkonian, M. Shedding light on vampires: the phylogeny of vampyrellid amoebae revisited. *PLoS One* **7**, e31165 (2012).
5. Ley, K., Laudanna, C., Cybulsky, M. I. & Nourshargh, S. Getting to the site of inflammation: the leukocyte adhesion cascade updated. *Nat. Rev. Immunol.* **7**, 678–689 (2007).
6. Crossley, V. A. A literature review on the design of spherical rolling robots. *Pittsburgh, Pa* 1–6 (2006).
7. Ortigoza, R. S. *et al.* Wheeled mobile robots: a review. *IEEE Lat. Am. Transactions* **10**, 2209–2217 (2012).
8. Taylor, G. I. Analysis of the swimming of microscopic organisms. *Proc. Royal Soc. London. Ser. A. Math. Phys. Sci.* **209**, 447–461 (1951).
9. Purcell, E. M. Life at low reynolds number. *Am. journal physics* **45**, 3–11 (1977).
10. Wang, Q. & Zhang, L. External power-driven microrobotic swarm: from fundamental understanding to imaging-guided delivery. *ACS nano* **15**, 149–174 (2021).
11. Xie, H. *et al.* Reconfigurable magnetic microrobot swarm: Multimode transformation, locomotion, and manipulation. *Sci. robotics* **4**, eaav8006 (2019).
12. Kaiser, A., Snezhko, A. & Aranson, I. S. Flocking ferromagnetic colloids. *Sci. advances* **3**, e1601469 (2017).
13. Ahmed, D. *et al.* Neutrophil-inspired propulsion in a combined acoustic and magnetic field. *Nat. communications* **8**, 1–8 (2017).
14. Alcântara, C. C. *et al.* Mechanically interlocked 3d multi-material micromachines. *Nat. communications* **11**, 1–8 (2020).
15. Dong, Y. *et al.* Magnetic helical micro-/nanomachines: Recent progress and perspective. *Matter* **5**, 77–109 (2022).
16. Liu, L. *et al.* Wireless manipulation of magnetic/piezoelectric micromotors for precise neural stem-like cell stimulation. *Adv. Funct. Mater.* **30**, 1910108 (2020).
17. Chamolly, A., Lauga, E. & Tottori, S. Irreversible hydrodynamic trapping by surface rollers. *Soft Matter* **16**, 2611–2620 (2020).
18. Bozuyuk, U., Alapan, Y., Aghakhani, A., Yunusa, M. & Sitti, M. Shape anisotropy-governed locomotion

of surface microrollers on vessel-like microtopographies against physiological flows. *Proc. Natl. Acad. Sci.* **118** (2021).

19. Ahmed, D. *et al.* Bioinspired acousto-magnetic microswarm robots with upstream motility. *Nat. machine intelligence* **3**, 116–124 (2021).
20. Li, T. *et al.* Dynamic thermal trapping enables cross-species smart nanoparticle swarms. *Sci. advances* **7**, eabe3184 (2021).
21. Tasci, T., Herson, P., Neeves, K. & Marr, D. Surface-enabled propulsion and control of colloidal microwheels. *Nat. communications* **7**, 1–6 (2016).
22. Yang, T. *et al.* Microwheels on microroads: Enhanced translation on topographic surfaces. *Sci. robotics* **4**, eaaw9525 (2019).
23. Baker, R. D. *et al.* Shape-programmed 3d printed swimming microtori for the transport of passive and active agents. *Nat. communications* **10**, 1–10 (2019).
24. Ressnerova, A. *et al.* Efficient protein transfection by swarms of chemically powered plasmonic virus-sized nanorobots. *ACS nano* **15**, 12899–12910 (2021).
25. Sánchez, S., Soler, L. & Katuri, J. Chemically powered micro-and nanomotors. *Angewandte Chemie Int. Ed.* **54**, 1414–1444 (2015).
26. Das, S. *et al.* Boundaries can steer active janus spheres. *Nat. communications* **6**, 1–10 (2015).
27. Medina-Sánchez, M., Magdanz, V., Guix, M., Fomin, V. M. & Schmidt, O. G. Swimming microrobots: Soft, reconfigurable, and smart. *Adv. Funct. Mater.* **28**, 1707228 (2018).
28. Park, B.-W., Zhuang, J., Yasa, O. & Sitti, M. Multifunctional bacteria-driven microswimmers for targeted active drug delivery. *ACS nano* **11**, 8910–8923 (2017).
29. Hosseinidoust, Z. *et al.* Bioengineered and biohybrid bacteria-based systems for drug delivery. *Adv. drug delivery reviews* **106**, 27–44 (2016).
30. Lim, B. *et al.* Magnetophoretic circuits for digital control of single particles and cells. *Nat. communications* **5**, 1–10 (2014).
31. Aziz, A., Holthof, J., Meyer, S., Schmidt, O. G. & Medina-Sánchez, M. Dual ultrasound and photoacoustic tracking of magnetically driven micromotors: From in vitro to in vivo. *Adv. Healthc. Mater.* **10**, 2101077 (2021).
32. Yang, T. *et al.* Reconfigurable microbots folded from simple colloidal chains. *Proc. Natl. Acad. Sci.* **117**, 18186–18193 (2020).
33. Cao, Q. *et al.* Recent advances in manipulation of micro-and nano-objects with magnetic fields at small scales. *Mater. Horizons* **7**, 638–666 (2020).
34. Lin, Z. *et al.* Magnetically actuated peanut colloid motors for cell manipulation and patterning. *Acs*

Nano **12**, 2539–2545 (2018).

35. Jeon, S. *et al.* Magnetically actuated microrobots as a platform for stem cell transplantation. *Sci. Robotics* **4**, eaav4317 (2019).
36. Zhou, H., Mayorga-Martinez, C. C. & Pumera, M. Microplastic removal and degradation by mussel-inspired adhesive magnetic/enzymatic microrobots. *Small Methods* **5**, 2100230 (2021).
37. Zhou, H., Mayorga-Martinez, C. C., Pané, S., Zhang, L. & Pumera, M. Magnetically driven micro and nanorobots. *Chem. Rev.* **121**, 4999–5041 (2021).
38. Yan, J. *et al.* Reconfiguring active particles by electrostatic imbalance. *Nat. materials* **15**, 1095–1099 (2016).
39. Liu, D., Yang, Z., Zhang, L., Wei, M. & Lu, Y. Cell-free biology using remote-controlled digital microfluidics for individual droplet control. *RSC Adv.* **10**, 26972–26981 (2020).
40. Palacci, J., Sacanna, S., Steinberg, A. P., Pine, D. J. & Chaikin, P. M. Living crystals of light-activated colloidal surfers. *Science* **339**, 936–940 (2013).
41. Palagi, S. *et al.* Structured light enables biomimetic swimming and versatile locomotion of photoresponsive soft microrobots. *Nat. materials* **15**, 647–653 (2016).
42. Urso, M., Ussia, M. & Pumera, M. Breaking polymer chains with self-propelled light-controlled navigable hematite microrobots. *Adv. Funct. Mater.* **31**, 2101510 (2021).
43. Jiang, H.-R., Yoshinaga, N. & Sano, M. Active motion of a janus particle by self-thermophoresis in a defocused laser beam. *Phys. review letters* **105**, 268302 (2010).
44. Maggi, C., Saglimbeni, F., Dipalo, M., De Angelis, F. & Di Leonardo, R. Micromotors with asymmetric shape that efficiently convert light into work by thermocapillary effects. *Nat. communications* **6**, 1–5 (2015).
45. Ahmed, D. *et al.* Artificial swimmers propelled by acoustically activated flagella. *Nano letters* **16**, 4968–4974 (2016).
46. Guo, F. *et al.* Three-dimensional manipulation of single cells using surface acoustic waves. *Proc. Natl. Acad. Sci.* **113**, 1522–1527 (2016).
47. Lu, X. *et al.* Topographical manipulation of microparticles and cells with acoustic microstreaming. *ACS applied materials & interfaces* **9**, 38870–38876 (2017).
48. Hou, Z., Zhou, Z., Liu, P. & Pei, Y. Robotic trajectories and morphology manipulation of single particle and granular materials by a vibration tweezer. *Soft Robotics* **8**, 1–9 (2021).
49. Meng, L. *et al.* Acoustic tweezers. *J. Phys. D: Appl. Phys.* **52**, 273001 (2019).
50. Aghakhani, A., Yasa, O., Wrede, P. & Sitti, M. Acoustically powered surface-slipping mobile microrobots. *Proc. Natl. Acad. Sci.* **117**, 3469–3477 (2020).

51. Ahmed, D. *et al.* Selectively manipulable acoustic-powered microswimmers. *Sci. reports* **5**, 1–8 (2015).
52. Wang, W., Castro, L. A., Hoyos, M. & Mallouk, T. E. Autonomous motion of metallic microrods propelled by ultrasound. *ACS nano* **6**, 6122–6132 (2012).
53. Go, G. *et al.* Human adipose–derived mesenchymal stem cell–based medical microrobot system for knee cartilage regeneration in vivo. *Sci. Robotics* **5**, eaay6626 (2020).
54. Wu, Z. *et al.* A swarm of slippery micropropellers penetrates the vitreous body of the eye. *Sci. advances* **4**, eaat4388 (2018).
55. Singh, A. V. *et al.* Multifunctional magnetic hairbot for untethered osteogenesis, ultrasound contrast imaging and drug delivery. *Biomaterials* **219**, 119394 (2019).
56. Lo, W.-C., Fan, C.-H., Ho, Y.-J., Lin, C.-W. & Yeh, C.-K. Tornado-inspired acoustic vortex tweezer for trapping and manipulating microbubbles. *Proc. Natl. Acad. Sci.* **118** (2021).
57. Sun, M. *et al.* Swarming microdroplets to a dexterous micromanipulator. *Adv. Funct. Mater.* **31**, 2011193 (2021).
58. Cavalleri, G., Spavieri, G. & Spinelli, G. The ampere and biot-savart force laws. *european J. Phys.* **17**, 205 (1996).
59. Marzo, A. *et al.* Holographic acoustic elements for manipulation of levitated objects. *Nat. communications* **6**, 1–7 (2015).
60. Marzo, A. & Drinkwater, B. W. Holographic acoustic tweezers. *Proc. Natl. Acad. Sci.* **116**, 84–89 (2019).
61. Zhong, C., Jia, Y., Jeong, D. C., Guo, Y. & Liu, S. Acousnet: A deep learning based approach to dynamic 3d holographic acoustic field generation from phased transducer array. *IEEE Robotics Autom. Lett.* **7**, 666–673 (2021).
62. King, L. V. On the acoustic radiation pressure on spheres. *Proc. Royal Soc. London. Ser. A-Mathematical Phys. Sci.* **147**, 212–240 (1934).
63. Gor'kov, L. P. On the forces acting on a small particle in an acoustical field in an ideal fluid. In *Sov. Phys. Dokl.*, vol. 6, 773–775 (1962).
64. Yosioka, K. & Kawasima, Y. Acoustic radiation pressure on a compressible sphere. *Acta Acustica united with Acustica* **5**, 167–173 (1955).
65. Dual, J. & Möller, D. Acoustofluidics 4: Piezoelectricity and application in the excitation of acoustic fields for ultrasonic particle manipulation. *Lab on a Chip* **12**, 506–514 (2012).
66. Schneider, C. A., Rasband, W. S. & Eliceiri, K. W. Nih image to imagej: 25 years of image analysis. *Nat. methods* **9**, 671–675 (2012).

Figures and Legends

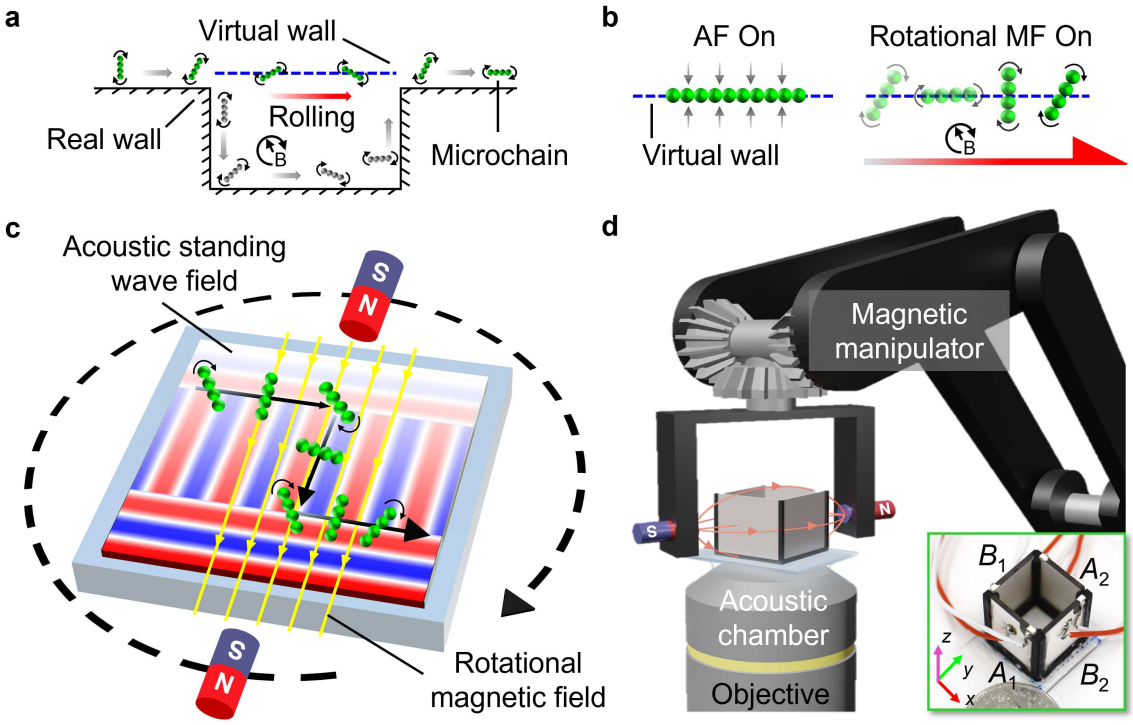

Fig. 1. Illustration of chain-shaped microswarms rolling along acoustic virtual walls. (**a**) Virtual wall concept. To move from left to right by means of rolling, the gray microchain (conventional method) has to follow the boundary posed by the real wall; in contrast, the green microchain (our strategy) can directly roll forward along the virtual wall. (**b**) Mechanism of microchain rolling along one-dimensional acoustic virtual walls. (i) Magnetic particles are pushed to the pressure nodal line by the acoustic radiation force as the acoustic standing wave field (AF) is developed. Gray arrows denote the acoustic virtual wall effect from both sides of the acoustic pressure nodal line, which is denoted by the blue dotted line. (ii) Magnetic particles assemble into microchains and achieve rolling motion along the acoustic virtual wall as soon as the rotational magnetic field (MF) is introduced. The curved black arrow indicates rotational direction. The red arrow shows the rolling direction. (**c**) Schematic of microchains rolling along two-dimensional dynamic acoustic virtual walls, realized by switching the orientation of the acoustic standing wave field and the rotational direction of the magnetic field. (**d**) Schematic of the experimental setup, consisting of an acoustic manipulation chamber and a magnetic manipulation system. The whole setup is mounted on an inverted microscope, and we image the rolling motion using high-speed and high-sensitivity cameras. The inset shows the piezoelectric transducer pairs $A_{1,2}$ and $B_{1,2}$.

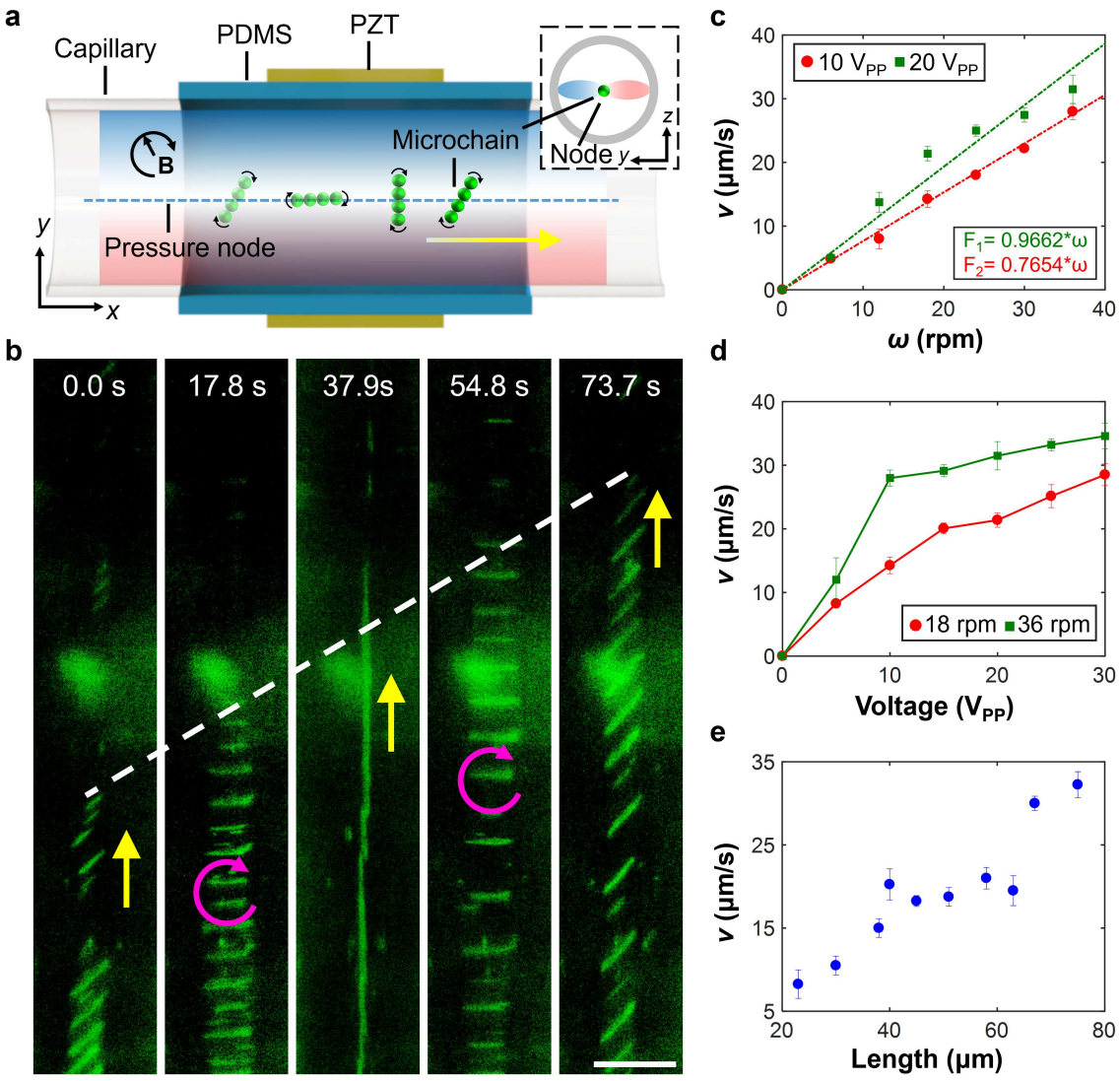

Fig. 2. Characterization of microchains rolling along the single acoustic virtual wall in a confined glass capillary. (**a**) Schematic of the experimental setup. The capillary is held by a polydimethylsiloxane (PDMS) polymer substrate with two piezoelectric transducers (PZT) attached on the substrate's lateral surfaces. The inset illustrates a cross-sectional view of the glass capillary with the microchain trapped at the pressure node of an acoustic standing wave field. (**b**) Image sequence of microchains rotating from bottom to top. The pink curved arrow, yellow arrow, and white dotted line respectively denote the clockwise magnetic rotational direction, net displacement direction and displacement. Scale bar, 100 μm. (**c**) Plot characterizing the translation velocity of a single microchain (length 65.63 μm) versus magnetic rotational velocity at selected acoustic voltages. The dotted lines are the corresponding linear fits. (**d**) Plot characterizing the translation velocity of the same single microchain versus acoustic voltage at selected magnetic rotational velocities. (**e**) Plot of the translation velocity versus microchain length under an acoustic excitation voltage and frequency of 20 V_{PP} and 2.02 MHz, respectively. The magnetic rotational velocity and the magnetic intensity were 24 rpm and 15 mT, respectively.

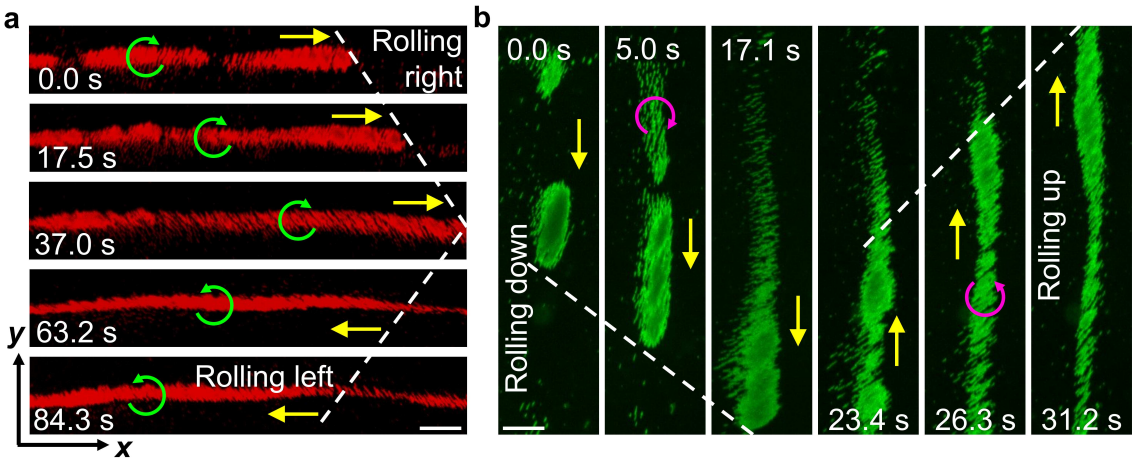

Fig. 3. Bidirectional rolling of microchains along the acoustic virtual wall. (**a**) Bidirectional rolling motion (the direction is indicated by a yellow arrow) along the x-axial acoustic virtual wall upon flipping the rotational direction of the magnetic field (green curved arrow). The white dotted line denotes the net displacement. (**b**) Bidirectional rolling motion along the y-axial acoustic virtual wall. The pink curved arrows denote the magnetic rotational direction. For both panels, the acoustic excitation voltage and frequency were 20 V_{PP} and 1.55 MHz, respectively. The magnetic rotational velocity and intensity were 24 rpm and 21 mT, respectively. Scale bar, 100 µm.

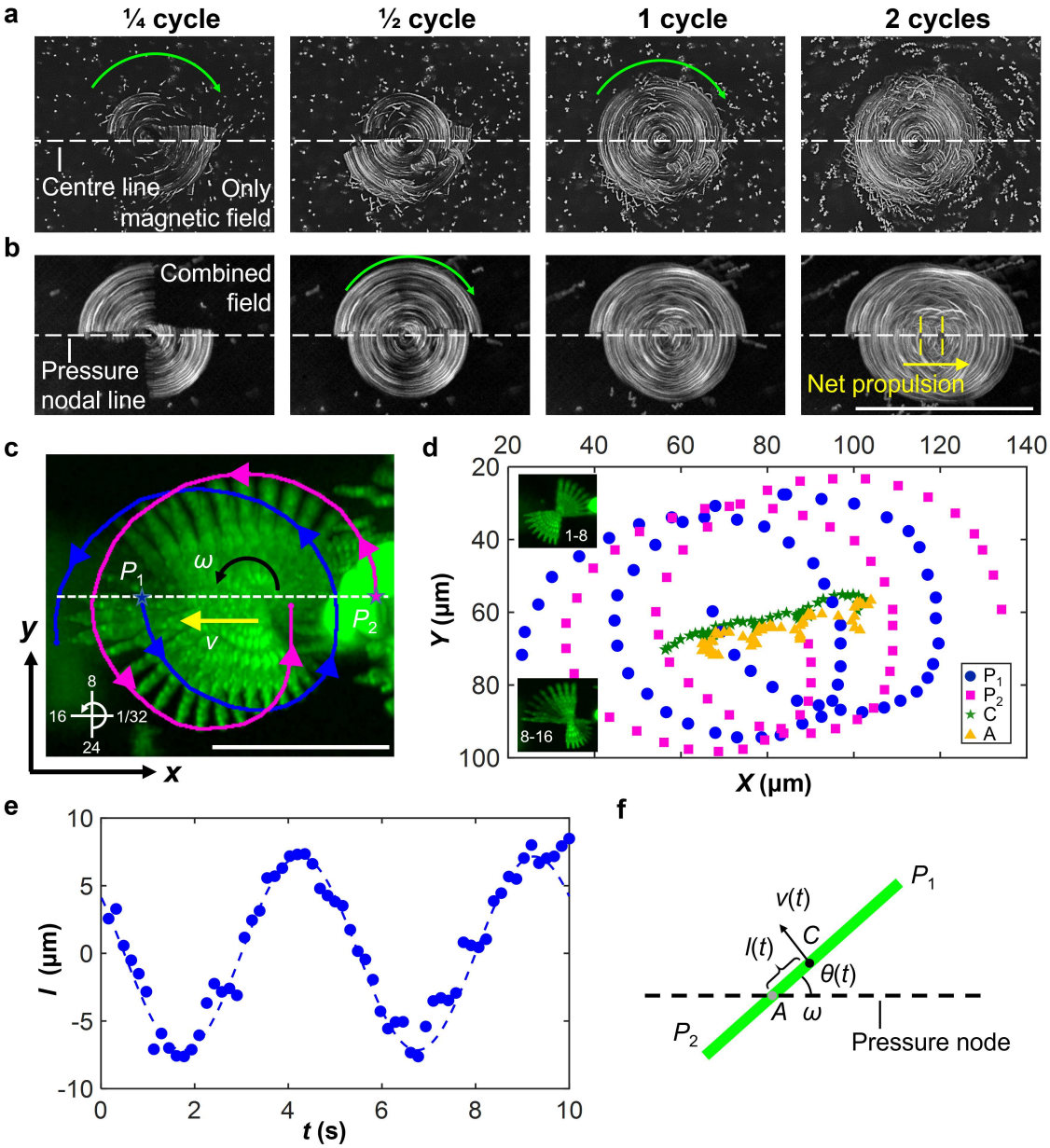

Fig. 4. Mechanism of rolling motion along the acoustic virtual wall. (**a**) Rotation of a microchain in the absence of an acoustic field. The 1/4-cycle superimposed subfigure shows off-center rotation of the microchain, while the 2-cycle subfigure shows its final rotational profile to be like a circle. No noticeable motion is observed. (**b**) Rotation of a microchain in the presence of a one-dimensional acoustic standing wave field. The microchain exhibits off-center rotation and rolling along the acoustic pressure nodal line. The white dotted lines of (**a**) and (**b**) respectively denote the rotational centerline and the acoustic pressure nodal line. The green curved arrow denotes the rotational direction. The yellow arrow and dotted line denote the rolling direction and the net displacement, respectively. Scale bar, 50 μm. (**c**) Superimposed time-lapse images of a microchain undergoing one rotational cycle. The acoustic excitation voltage and frequency were 20 V_{PP} and 1.55 MHz, respectively. The magnetic rotational direction was counterclockwise, and the magnetic rotational velocity and intensity were 12 rpm and 21 mT, respectively. Blue and pink curves respectively denote the tracked trajectories of the two endpoints, P_1 and P_2. The white dotted line denotes the acoustic pressure nodal line. Scale bar, 50 μm. (**d**) Trajectories of the microchain's two endpoints (P_1 and P_2), geometric center (C), and rotational center (A). The data of P_1 and P_2 was manually tracked across each frame of the recorded experimental video. The position of C was calculated as the center of the line P_1P_2. The position of A was manually tracked by superimposing adjacent frames of the recorded experimental video. (**e**) Plot of the variable distance between the geometric and rotational centers of the microchain against rotational time. The period of one rotational cycle was 5 seconds. The between-center distance was obtained by subtracting the distance $|P_1C|$ from $|P_1A|$. Fitting yielded a first-order sine function of $l(t) = 7.157 * \sin(1.256t + 2.518)$. (**f**) Schematic of the experiment-supported theoretical model. The green rod denotes the self-assembled microchain.

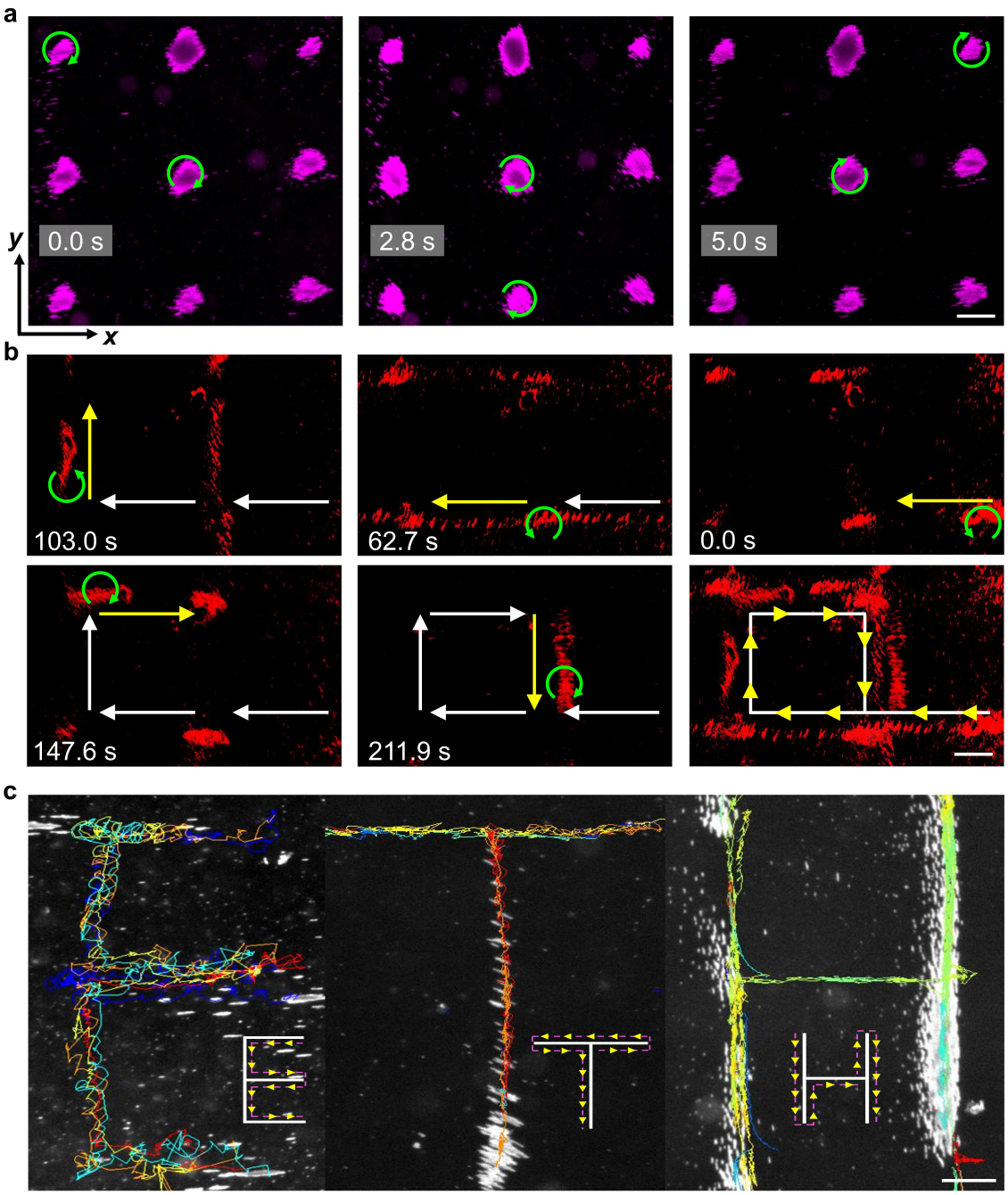

Fig. 5. Two-dimensional dynamic rolling manipulation. (**a**) *In situ* rotation of microchains at two-dimensional acoustic pressure nodal points. (**b**) Rolling of microchains along a predesigned square path. The last subfigure is a superimposed time-lapse image showing the full path. The green curved arrow, yellow arrow, and white arrow respectively denote rotational direction, rolling direction, and the historical path. (**c**) Using customizable acoustic virtual walls to write the word "*ETH*" with rolling microchains. Inset figures show the rolling direction. The acoustic excitation frequency was 1.55 MHz and the magnetic intensity was 21 mT, respectively. Scale bar, 100 μm.

Supplementary Files

This is a list of supplementary files associated with this preprint. Click to download.

- Movie1.mp4
- Movie2.mp4
- Movie3.mp4
- Movie4.mp4
- Movie5.mp4
- SupplementaryInformation.pdf